Evaluation of an Eulerian multi-material mixture formulation based on a single inverse deformation gradient tensor field

By N. S. Ghaisas, A. Subramaniam, S. K. Lele AND A. W. Cook†

1. Motivation and objectives

High-energy-density solids undergoing elastic-plastic deformations coupled to compressible fluids are a common occurrence in engineering applications. Examples include problems involving high-velocity impact and penetration, cavitation, and several manufacturing processes, such as cold forming. Numerical simulations of such phenomena require the ability to handle the interaction of shock waves with multi-material interfaces that can undergo large deformations and severe distortions. As opposed to Lagrangian (Benson 1992) and arbitrary Lagrangian-Eulerian (ALE) methods (Donea *et al.* 2004), fully Eulerian methods use grids that do not change in time. Consequently, Eulerian methods do not suffer from difficulties on account of mesh entanglement, and do not require periodic, expensive, remap operations. An extensive review of numerical issues associated with Lagrangian, ALE and Eulerian methods may be found in Benson (1992).

Eulerian methods for multi-material problems can be classified into either sharp-interface or diffuse-interface methods, depending on whether the interface width is comparable to the other scales in the flow and needs to be modeled explicitly. An advantage of diffuse-interface methods over sharp-interface methods is the property of conservation of mass. Furthermore, high-order, high-resolution numerical methods such as those based on compact finite differences, which are global in nature, can be applied more easily to the diffuse-interface formulation.

Recent applications of the diffuse-interface method to solid-solid and solid-fluid interfaces include those of Favrie & Gavrilyuk (2012) and Ndanou *et al.* (2015). These formulations build on the underlying formulations for tracking large, elastic-plastic deformations in a single hyperelastic solid (Plohr & Sharp 1989; Godunov & Romenskii 2003). In particular, Trangenstein & Colella (1991) and Miller & Colella (2001) use the inverse deformation gradient tensor as the basic kinematic variable to track deformations of solids. The diffuse-interface solid-fluid method of Favrie & Gavrilyuk (2012) and Ndanou *et al.* (2015) used a second-order Godunov-type numerical framework. In our previous work, a high-order numerical framework, previously applied to fluid problems, was extended to problems involving large deformations of solids (Subramaniam *et al.* 2017).

The diffuse-interface multi-solid, multi-fluid formulation of Favrie & Gavrilyuk (2012), Ndanou *et al.* (2015) and Subramaniam *et al.* (2017) makes use of one field of inverse deformation gradient tensor per species. The total number of transport equations is $10M+4$

† Lawrence Livermore National Laboratory, Livermore CA

for a system involving M materials. This formulation is likely to be prohibitively expensive, even for moderate M. The aim of this paper is to develop a reduced multi-material formulation, capable of handling large deformations of solids and flow of fluids. The cost saving comes from the use of a single inverse deformation gradient tensor field, instead of material-specific tensor fields. This mixture multi-material formulation is developed and evaluated in this paper.

Details of the full (multiple-g) and proposed reduced (mixture) formulations are given in Section 2. The errors in the mixture formulation with respect to the multiple-g formulation are investigated in detail for several test problems in Section 3. Convergence of the mixture formulation is studied in Section 4, along with a demonstration of the applicability of the mixture formulation to a problem of practical engineering interest, namely, the classical Taylor impact problem. Section 5 concludes the paper.

2. Eulerian multi-material formulations

2.1. *Multiple-g formulation*

The fundamental Eulerian equations governing the motion of a multi-material continuum are the species mass, momentum and total energy conservation equations,

$$\frac{\partial \rho Y_m}{\partial t} + \frac{\partial \rho Y_m u_k}{\partial x_k} = -\frac{\partial (J^*_m)_i}{\partial x_i}, \tag{2.1}$$

$$\frac{\partial \rho u_i}{\partial t} + \frac{\partial}{\partial x_k}\left[\rho u_i u_k - \sigma_{ik}\right] = \frac{\partial \tau^*_{ik}}{\partial x_k}, \tag{2.2}$$

$$\frac{\partial}{\partial t}\left[\rho\left(\varepsilon + \frac{1}{2}u_j u_j\right)\right] + \frac{\partial}{\partial x_k}\left[\rho u_k\left(\varepsilon + \frac{1}{2}u_j u_j\right) - \sigma_{ik}u_i\right] = \frac{\partial}{\partial x_k}\left[\tau^*_{ik}u_i - q^*_k\right]. \tag{2.3}$$

$\boldsymbol{u}$ is the velocity and Y_m is the mass fraction of material m. ρ, ε and $\underline{\boldsymbol{\sigma}}$ are the continuum density, internal energy and Cauchy stress, respectively, given in terms of species-specific quantities ρ_m, ε_m and $\underline{\boldsymbol{\sigma}}_m$ by

$$\rho = \sum_{m=1}^{M} \alpha_m \rho_m, \quad \varepsilon = \sum_{m=1}^{M} Y_m \varepsilon_m, \quad \underline{\boldsymbol{\sigma}} = \sum_{m=1}^{M} \alpha_m \underline{\boldsymbol{\sigma}}_m, \tag{2.4}$$

where α_m is the volume fraction of material m and M is the total number of materials. The volume fractions satisfy the constraint $\sum_{m=1}^{M} \alpha_m = 1$. The artificial viscous stress $\tau^*_{ik} = 2\mu^* S_{ik} + (\beta^* - 2\mu^*/3)\,(\partial u_j/\partial x_j)\,\delta_{ik}$, and the artificial heat flux $q^*_i = -\kappa^* \partial T/\partial x_i + \sum_{m=1}^{M} h_m\,(J^*_m)_i$. $S_{ik} = (\partial u_i/\partial x_k + \partial u_k/\partial x_i)/2$ is the strain rate tensor, T is the temperature and μ^*, β^* and κ^* are the artificial shear viscosity, artificial bulk viscosity and artificial thermal conductivity, respectively. The form of artificial properties used here is the same as in Ghaisas *et al.* (2016). The second term in the expression for q^*_i is the enthalpy diffusion term (Cook 2009), where $h_m = \varepsilon_m + p_m/\rho_m$ is the enthalpy of species m. $(J^*_m)_i = -\rho\left[D^*_m\,(\partial Y_m/\partial x_i) - Y_m \sum_k D^*_k\,(\partial Y_k/\partial x_i)\right]$ is the Fickian diffusive flux for species m in direction x_i and D^*_m is the artificial diffusivity of species m. The form for D^*_m is the same as that used in Subramaniam *et al.* (2017).

The above system of conservation equations is complemented by kinematic equations governing the elastic part of the inverse deformation gradient tensor, $\underline{\boldsymbol{g}}^e_m$, for each material

m, as written in López Ortega *et al.* (2014); Ndanou *et al.* (2015) as

$$\frac{\partial (g^e_m)_{ij}}{\partial t} + \frac{\partial u_k (g^e_m)_{ik}}{\partial x_j} = u_k \left[\frac{\partial (g^e_m)_{ik}}{\partial x_j} - \frac{\partial (g^e_m)_{ij}}{\partial x_k} \right] + \zeta_g \left(\frac{\rho_m}{\rho_{0,m} |\underline{\boldsymbol{g}}_m|} - 1 \right) (g^e_m)_{ij} + \frac{1}{2\mu_m \left(\frac{\rho_m}{\rho_{0,m}} \right) \tau_{0,m}} \left[\frac{\mathrm{R}\left(||\underline{\boldsymbol{\sigma}}'_m||^2 - \frac{2}{3}\sigma^2_{Y,m} \right)}{\mu^2_m} \right] (g^e_m)_{ik} \, \sigma'_{kj}. \quad (2.5)$$

The standard multiplicative decomposition, $\underline{\boldsymbol{g}} = \underline{\boldsymbol{g}}^p \underline{\boldsymbol{g}}^e$, has been used to derive these equations, where $\underline{\boldsymbol{g}}^p$ denotes the plastic part of the inverse deformation gradient tensor. The second term on the right-hand side is to ensure consistency with the material density, and $\zeta_g = 1/(6\Delta t)$ is a time step-dependent constant (Miller & Colella 2001). The last term on the right-hand side of Eq. (2.5) accounts for plasticity effects, where μ_m denotes the shear modulus, $\rho_{0,m}$ denotes the density in the undeformed state, and $\underline{\boldsymbol{\sigma}}'_m = \underline{\boldsymbol{\sigma}}_m - (\mathrm{tr}\,(\underline{\boldsymbol{\sigma}}_m)/3)\,\underline{\boldsymbol{I}}$ is the deviatoric part of $\underline{\boldsymbol{\sigma}}_m$. The yield stress is denoted by $\sigma_{Y,m}$, and $1/\tau_{0,m}$ is the inverse of the plastic relaxation timescale of material m. The Ramp function, $\mathrm{R}(x) = x$ if $x > 0$ and 0 otherwise, turns off plasticity effects whenever the deviatoric stress contraction is below the yield stress; i.e. $||\underline{\boldsymbol{\sigma}}'_m||^2 = \sigma'_{ij,m}\sigma'_{ij,m} < (2/3)\,\sigma^2_{Y,m}$.

The above formulation requires an equation of state (EOS) for each material, that relates the stresses and strains. We consider a classical hyperelastic EOS, without additional contributions due to capillary/Korteweg effects. The stress is derived from an energy functional based on thermodynamic consistency through the Clausius-Duhem inequality. The internal energy and the Cauchy stress of material m are given by

$$\varepsilon_m = \frac{p + \gamma_m p_{\infty,m}}{(\gamma_m - 1)\,\rho_m} + \frac{\mu_m}{4\rho_{0,m}} \mathrm{tr}\left[\left(\underline{\boldsymbol{g}}^e_m - \underline{\boldsymbol{I}} \right)^2 \right], \quad (2.6)$$

$$\underline{\boldsymbol{\sigma}}_m = -p\underline{\boldsymbol{I}} - \mu_m \left[|\underline{\boldsymbol{G}}_m|^{-1/6} \left(\underline{\boldsymbol{G}}^2_m \right)' - |\underline{\boldsymbol{G}}_m|^{1/6} \left(\underline{\boldsymbol{G}}_m \right)' \right], \quad (2.7)$$

where $\underline{\boldsymbol{G}}_m = \left(\underline{\boldsymbol{g}}^e_m \right)^T \underline{\boldsymbol{g}}^e_m$ is the elastic Finger tensor and $\underline{\boldsymbol{I}}$ is the identity tensor. Material behavior is described by EOS parameters, γ_m and $p_{\infty,m}$, shear modulus, μ_m, and the undeformed density, $\rho_{0,m}$. This constitutive description is the same as in Subramaniam *et al.* (2017) and Ndanou *et al.* (2015). Note that this constitutive description can be used to model solids ($\mu_m \neq 0$, $p_{\infty,m} \neq 0$), liquids ($\mu_m = 0$, $p_{\infty,m} \neq 0$) and gases ($\mu_m = 0$, $p_{\infty,m} = 0$). All materials are assumed to be in thermal and mechanical equilibrium, and hence, have identical pressure, p, and temperature, T.

The complete set of equations, Eqs. (2.1)-(2.7), comprises of a total of $10M + 4$ partial differential equations for a system of M materials. Since it involves an inverse deformation gradient tensor for each material, it is referred to as the multiple-g formulation.

2.2. *Mixture formulation*

We consider a reduced formulation that involves a single elastic inverse deformation gradient tensor field, $\underline{\boldsymbol{g}}^e$, in place of material-specific fields, $\underline{\boldsymbol{g}}^e_m$. The equations governing

the evolution of the mixture $\underline{\boldsymbol{g}}^e$ field are taken to be

$$\frac{\partial (g^e)_{ij}}{\partial t} + \frac{\partial u_k (g^e)_{ik}}{\partial x_j} = u_k \left[\frac{\partial (g^e)_{ik}}{\partial x_j} - \frac{\partial (g^e)_{ij}}{\partial x_k} \right] + \zeta_g \left(\frac{\rho}{\rho_{0,mix} |\underline{\boldsymbol{g}}|} - 1 \right) (g^e)_{ij} + \frac{1}{2\mu_{mix} \left(\frac{\rho}{\rho_{0,mix}} \right) \tau_{0,mix}} \left[\frac{\mathrm{R} \left(||\underline{\boldsymbol{\sigma}}'_{mix}||^2 - \frac{2}{3}\sigma^2_{Y,mix} \right)}{\mu^2_{mix}} \right] (g^e)_{ik} \, \sigma'_{mix,kj}. \tag{2.8}$$

The mixture reference density, mixture shear modulus, mixture yield stress and mixture plastic relaxation timescale are given as volume fraction-weighted sums of material-specific properties

$$\rho_{0,mix} = \sum_{m=1}^{M} \alpha_m \rho_{0,m}, \quad \mu_{mix} = \sum_{m=1}^{M} \alpha_m \mu_m, \quad \sigma_{Y,mix} = \sum_{m=1}^{M} \alpha_m \sigma_m, \quad \tau_{0,mix} = \sum_{m=1}^{M} \alpha_m \tau_{0,m}. \tag{2.9}$$

Analogous to Eqs. (2.6)-(2.7), the mixture constitutive relations are assumed to be

$$\varepsilon_{mix} = \sum_{m=1}^{M} Y_m \frac{p + \gamma_m p_{\infty,m}}{(\gamma_m - 1)\, \rho_m} + \frac{\mu_{mix}}{4\rho_{0,mix}} \mathrm{tr} \left[\left(\underline{\boldsymbol{g}}^e - \underline{\boldsymbol{I}} \right)^2 \right], \tag{2.10}$$

$$\underline{\boldsymbol{\sigma}}_{mix} = -p\underline{\boldsymbol{I}} - \mu_{mix} \left[|\underline{\boldsymbol{G}}|^{-1/6} \left(\underline{\boldsymbol{G}}^2 \right)' - |\underline{\boldsymbol{G}}|^{1/6} \left(\underline{\boldsymbol{G}} \right)' \right]. \tag{2.11}$$

In summary, the reduced formulation proposed here is composed of Eqs. (2.1)-(2.3) with ε_{mix} and $\underline{\boldsymbol{\sigma}}_{mix}$ substituted in place of ε and $\underline{\boldsymbol{\sigma}}$, respectively; kinematic equations (Eq. (2.8)); constitutive relations (Eqs. (2.10)-(2.11)); and mixture rules (Eq. (2.9)). This formulation involves $M + 13$ equations for a system of M materials, and is termed the mixture formulation.

2.3. *Numerical solution procedure*

The multiple-g and mixture formulations outlined above are solved on a fixed Eulerian structured grid using a tenth-order compact finite-difference scheme (Lele 1992). The centered compact schemes used here have no inherent dissipation. Dissipation required for shock and interface capturing is added explicitly through the artificial viscous stress, artificial conductive flux and artificial diffusive flux in Eqs. (2.1)-(2.3). A fourth-order five-stage Runge-Kutta time integrator (Kennedy *et al.* 2000) is used. The plastic relaxation timescales for all materials are assumed to be much smaller than the other timescales in this paper, $\tau_{0,m} \ll 1$. The resulting stiff plastic source terms are integrated implicitly, following the method detailed by Favrie & Gavrilyuk (2010). The pressures and temperatures of different species are equilibrated at each grid point using the method outlined by Subramaniam *et al.* (2017). After each stage, the conserved variables are filtered for de-aliasing using an eighth-order compact filter (Cook & Cabot 2005). Further details may be found in Ghaisas *et al.* (2016) and Subramaniam *et al.* (2017).

3. Evaluation of mixture formulation

The mixture formulation is compared to the multiple-g formulation in this section for several test problems. We consider the multiple-g formulation to provide benchmark results, and denote the differences between mixture and multiple-g results as errors. It should be noted that the errors are being assessed not against an exact solution, but

against results generated by another numerical method, which itself introduces some numerical errors. Convergence and order-of-accuracy tests with an exact analytical solution and with respect to an experiment are relegated to the next section. Here, the mixture formulation results are benchmarked against the multiple-g formulation results for non-dynamic as well as dynamic problems below.

3.1. *Static tests*

The errors introduced by the constitutive relations in the mixture formulation with respect to the multiple-g formulation are examined first, for a given state of deformations. From Eqs. (2.4), (2.6)-(2.7) and (2.9)-(2.11), it is clear that

$$\tilde{\varepsilon}_{err} = \varepsilon_{mix} - \varepsilon = \frac{\mu_{mix}}{\rho_{0,mix}} h\left(\underline{\boldsymbol{g}}^e\right) - \sum_{m=1}^{M} Y_m \frac{\mu_m}{\rho_{0,m}} h\left(\underline{\boldsymbol{g}}^e_m\right), \tag{3.1}$$

$$\underline{\tilde{\boldsymbol{\sigma}}}_{err} = \underline{\boldsymbol{\sigma}}_{mix} - \underline{\boldsymbol{\sigma}} = -\mu_{mix} \underline{\boldsymbol{f}}\left(\underline{\boldsymbol{g}}^e\right) + \sum_{m=1}^{M} \alpha_m \mu_m \underline{\boldsymbol{f}}\left(\underline{\boldsymbol{g}}^e_m\right). \tag{3.2}$$

Here, $h\left(\underline{\boldsymbol{g}}^e\right)$ is the function occurring in Eqs. (2.6) and (2.10), and $\underline{\boldsymbol{f}}\left(\underline{\boldsymbol{g}}^e\right)$ is the tensor function of a tensor occurring in Eqs. (2.7) and (2.11). For problems involving materials with identical values of $\sigma_{Y,m}/\mu_m$, and identical values of the plastic relaxation timescale, $\tau_{0,m}$, the inverse deformation gradient fields are analytically identical. This includes purely elastic problems, since $\sigma_{Y,m}/\mu_m \to \infty$ for such problems. For simplicity, we consider a system with only two materials; i.e. $M = 2$. The implications of the analysis below apply equally for systems with $M > 2$. For the special case of $\underline{\boldsymbol{g}}^e_1 \equiv \underline{\boldsymbol{g}}^e_2 \equiv \underline{\boldsymbol{g}}^e$, normalized errors can be defined as

$$\varepsilon_{err} = \tilde{\varepsilon}_{err}/h\left(\underline{\boldsymbol{g}}^e\right) = \frac{\mu_{mix}}{\rho_{0,mix}} - \sum_{m=1}^{M} Y_m \frac{\mu_m}{\rho_{0,m}}, \tag{3.3}$$

$$\sigma_{err} = \left(\underline{\tilde{\boldsymbol{\sigma}}}_{err} : \underline{\boldsymbol{f}}\right) / \left(\underline{\boldsymbol{f}} : \underline{\boldsymbol{f}}\right) = -\mu_{mix} + \sum_{m=1}^{M} \alpha_m \mu_m. \tag{3.4}$$

It is easy to see that $\sigma_{err} = 0$. Substituting $Y_m = \alpha_m \rho_m/\rho$ and $\rho_m = \rho_{0,m}\left(|\underline{\boldsymbol{g}}^e| + \epsilon_m\right)$, then

$$\varepsilon_{err} = \frac{\mu_{mix}}{\rho_{0,mix}} - \frac{\mu_{mix}|\underline{\boldsymbol{g}}^e| + (\alpha_1\mu_1\epsilon_1 + \alpha_2\mu_2\epsilon_2)}{\rho_{0,mix}|\underline{\boldsymbol{g}}^e| + (\alpha_1\rho_{0,1}\epsilon_1 + \alpha_2\rho_{0,2}\epsilon_2)}. \tag{3.5}$$

Here, ϵ_m (distinct from the energy, ε_m) denotes the mass-consistency error, or the mismatch between the actual species density and that implied by the $\underline{\boldsymbol{g}}_m$ and $\rho_{0,m}$ for material m. Analytically, $\epsilon_1 \equiv \epsilon_2 \equiv 0$, and $\varepsilon_{err} \equiv 0$, while in simulations, numerical errors almost always lead to non-zero mass-consistency errors.

In summary, errors are introduced in the mixture formulation for two reasons, namely, (1) material properties that lead to non-identical $\underline{\boldsymbol{g}}^e_m$ fields, and (2) numerically-induced mass-consistency errors, that lead to non-zero errors in energy.

The effect of various parameters on the errors in energy is summarized in Figure 1. We consider two materials, with non-dimensional parameters $\mu_1 = 1$, $\mu_2 = R_\mu$, $\rho_{0,1} = 1$ and $\rho_{0,2} = R_\rho$. For a fixed choice of $R_\rho = 10$ and $R_\mu = 40$, contours of ϵ_{err} are plotted in Figures 1(a,b) with $\epsilon_1/|\underline{\boldsymbol{g}}^e|, \epsilon_2/|\underline{\boldsymbol{g}}^e|$ varying up to 20%, for different values of α_1. In each case, $\alpha_2 = 1 - \alpha_1$. The errors are identically zero if $\epsilon_1 = \epsilon_2$, and increase with the difference $|\epsilon_1 - \epsilon_2|$. Furthermore, the errors are small whenever the continuum approaches

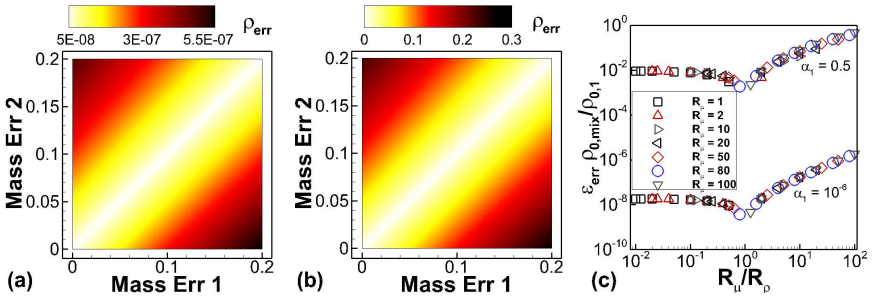

FIGURE 1. Contours of ε_{err}, deduced from Eq. (3.5), for varying mass-consistency errors, $\epsilon_1/|\underline{\boldsymbol{g}}^e|$ and $\epsilon_2/|\underline{\boldsymbol{g}}^e|$, with fixed material property ratios $R_\rho = 10$ and $R_\mu = 40$, and with (a) $\alpha_1 = 10^{-6}$, and (b) $\alpha_1 = 0.5$. $\alpha_2 = 1 - \alpha_1$. Note the contours range from 0 to (a) 6×10^{-7}, and (b) 0.03. (c) Profiles of ε_{err} for fixed $\epsilon_1/|\underline{\boldsymbol{g}}^e| = 0.05$, $\epsilon_2/|\underline{\boldsymbol{g}}^e| = 0.07$, varying property ratios R_ρ and $R_\mu = 1, 2, 10, 20, 50, 80$ and 100, and varying volume fractions.

a pure material; i.e. $\min(\alpha_1, \alpha_2)$ is close to zero. The errors are larger in mixture regions, where both materials have significant volume fractions.

Figure 1(c) shows the errors for fixed $\epsilon_1/|\underline{\boldsymbol{g}}^e| = 5\%$ and $\epsilon_2/|\underline{\boldsymbol{g}}^e| = 7\%$, and varying density and shear modulus ratios. For a fixed α_1, the errors collapse to a single curve when normalized by $\rho_{0,mix}/\rho_{0,1}$, and plotted against the ratio R_μ/R_ρ. Figure 1(c) represents the effect of material properties succinctly. Such plots can be used to assess the expected error, given material properties, volume fractions and mass-consistency errors.

3.2. *Spatial distribution and time evolution of errors*

The spatial distribution and temporal evolution of errors in three dynamic problems is considered next.

The first test problem involves materials with properties $\gamma_1 = \gamma_2 = 1.4$, $p_{\infty,1} = p_{\infty,2} = 1$, $\mu_1 = 1$, $\mu_2 = R_\mu$, $\sigma_{Y,1} = \sigma_{Y,2} = 0.01$ and $\rho_{0,1} = 1$, $\rho_{0,2} = R_\rho$. These values are obtained by non-dimensionalizing with $p_{\infty,1}$ and $\rho_{0,1}$ as pressure and density scales. The domain is periodic over $x \in [0, 1)$, with material 1 ranging over $x \in [0.5, 0.9]$. The interface is described by the initial volume fraction field, $\alpha_1 = \alpha_{min} + (1 - 2\alpha_{min})\,\chi(x)$, and $\alpha_2 = 1 - \alpha_1$, where $\chi(x) = 0.5\,[\mathrm{erf}\{(x - 0.5)\,/\,(\delta_t \Delta x)\} - \mathrm{erf}\{(x - 0.9)\,/\,(\delta_t \Delta x)\}]$. $\Delta x = 1/NX$ is the grid spacing. The values $\alpha_{min} = 10^{-6}$, $\delta_t = 1$ and $NX = 201$ are used. The velocities are zero everywhere initially. All inverse deformation gradient fields are $g_{11} = 1.1$, $g_{22} = 1.1\,[1 + 9\omega(x)]$ and $g_{33} = 1.1/\,[1 + 9\omega(x)]$, with $\omega(x) = (1/25)\exp[-128\,(x - 0.4)^2]$.

Non-linear waves that are initially smooth, but may steepen over time into shocks, are generated as the material relaxes from this initially strained condition. The mixture and multiple-g formulation results along with differences between the two at $t = 0.4$ are shown in Figure 2. For density and energy, the errors are concentrated near the interface. The errors in density and energy away from the interface and those in velocity and normal stress are dominated by spurious dispersive waves that are present in both the mixture and multiple-g formulations.

The second problem involves elastic-plastic shocks arising due to impact of two materials at $x = 0.5$. The domain is $x \in [0, 1]$, with non-periodic boundary conditions at the two ends. The simulation is stopped before the shocks reach the boundaries. The material properties are $\gamma_1 = \gamma_2 = 2.84$, $p_{\infty,1} = p_{\infty,2} = 1$, $\mu_1 = 1$, $\mu_2 = R_\mu$, $\sigma_{Y,1} = \sigma_{Y,2} = 0.1$ and $\rho_{0,1} = 1$, $\rho_{0,2} = R_\rho$. The initial volume fractions and velocities

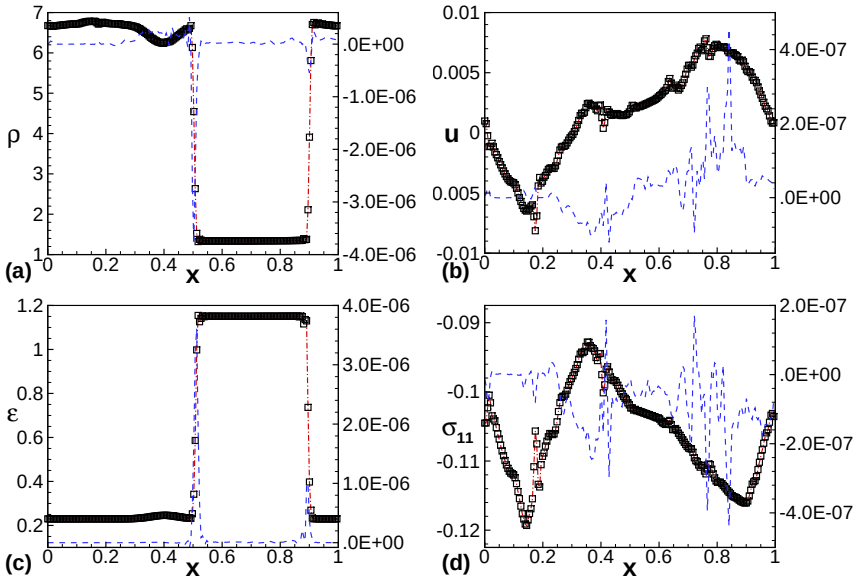

FIGURE 2. Relaxation from an initially strained condition for material property ratios $R_\rho = 5$ and $R_\mu = 1$. Profiles of non-dimensional (a) density, (b) velocity, (c) energy and (d) normal stress are shown at non-dimensional $t = 0.4$. Square symbols: mixture; dash-dotted lines: multiple-g; dashed lines: difference between mixture and multiple-g formulations, with labels on the right axes in each panel.

are given by $\alpha_1 = \alpha_{min} + (1 - 2\alpha_{min})\,\chi(x)$, $\alpha_2 = 1 - \alpha_1$ and $u = 0.5 - \chi(x)$, with $\chi(x) = 0.5\,[1 - \mathrm{erf}\,\{(x - 0.5)\,/\,(\delta_t \Delta x)\}]$. The numerical parameters are $\alpha_{min} = 10^{-6}$, $\delta_t = 2$ and $NX = 101$.

Figure 3 shows the mixture and multiple-g formulation results along with differences between the two at $t = 0.15$ for $R_\rho = 1$ and $R_\mu = 2$. The elastic precursor is distinct from the plastic wave in material 1 (to the left of the interface at $x = 0.5$), while the elastic and plastic waves are not distinctly visible in material 2. The errors are several orders of magnitude smaller than the quantities of interest, which are of order unity. The errors in density and energy are, again, largest close to the interface at all times. The errors in velocity and normal stress are significant over most of the domain influenced by the shocks, with distinct peaks at the locations of the shocks. The dispersive errors caused by spurious waves in the multiple-g and mixture formulations are seen in the close-up views of the velocity and normal stress profiles in Figures 3(e-f). The dispersive errors in the multiple-g result themselves contribute to the errors shown in Figure 3(a-d).

The last problem is the interaction between a shock and an interface between copper (Cu) and aluminum (Al) with a single-mode perturbation initially. This shock-interface interaction leads to two-dimensional distortion of the interface due to the Richtmyer-Meshkov instability mechanism (Brouillette 2002). The domain size, initial and boundary conditions are as described in Subramaniam *et al.* (2017). The interface grows linearly after the first interaction with the shock, while strong non-linear growth, along with roll-up of the interface and formation of distinct spikes and bubbles, is observed after interactions with the second and subsequent shocks reflected from the right wall. The material properties are $\gamma = 2$, $p_\infty = 68.23$ GPa, $\mu = 39.38$ GPa, $\sigma_Y = 0.12$ GPa and $\rho_0 = 8930$ kg/m^3 for Cu and $\gamma = 2.088$, $p_\infty = 32.98$ GPa, $\mu = 27.09$ GPa, $\sigma_Y = 0.297$

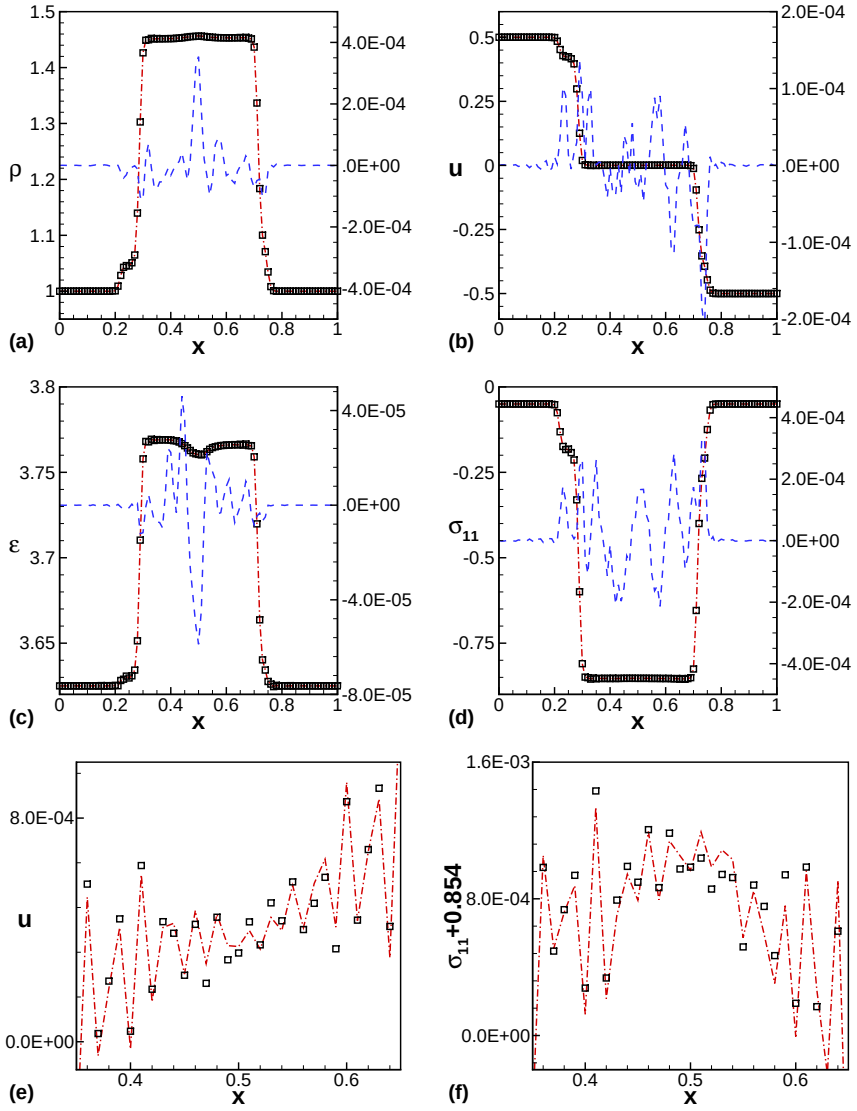

FIGURE 3. Elastic-plastic impact problem for material property ratios $R_\rho = 1$ and $R_\mu = 2$. Profiles of non-dimensional (a) density, (b) velocity, (c) energy and (d) normal stress at non-dimensional $t = 0.15$. Square symbols: mixture; dash-dotted lines: multiple-g; dashed lines: difference between mixture and multiple-g formulations, with labels on the right axes in (a-d). Close-up view of the dispersive errors over a portion of the domain in (e) velocity and (f) normal stress for the two formulations.

GPa and $\rho_0 = 2712$ kg/m^3 for Al. All quantities are non-dimensionalized by γp_∞ and ρ_0 for Cu. Numerical parameters used are $\alpha_{min} = 10^{-6}$, interface thickness $\delta_t = 3$, and grid size 384×64.

Contours of density at the final time, $t = 4$, obtained from the mixture and the multiple-g formulations are shown in Figure 4. The locations of the shock and entropy waves and the growth of the interface are very similar between the two results. Differences between the two formulations are also shown for different time points. It is clear that

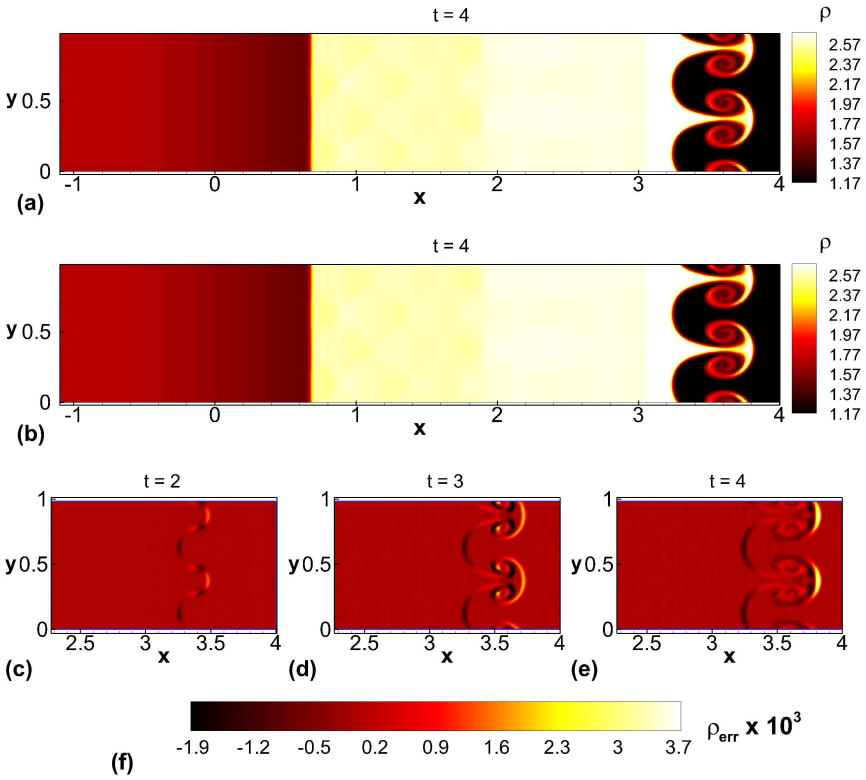

FIGURE 4. Richtmyer-Meshkov instability between elastic-plastic copper and aluminum. Contours of non-dimensional density from (a) mixture and (b) multiple-g formulations. Non-dimensional density errors at (c) $t = 2$, (d) $t = 3$ and (e) $t = 4$. (f) Contour legend for panels (c-e). Errors are smaller by three orders of magnitude than densities, and are concentrated near the interface.

differences in density are concentrated close to the interface, and are approximately three orders of magnitude smaller than the dynamic quantities. This test confirms that the spatial distribution trends observed in the one-dimensional problems hold for two-dimensional problems involving normal as well as shear waves, along with a significant distortion of the interface. The temporal evolution of errors in several quantities for the three problems described above is shown in Figure 5. It is clear that the errors do not grow exponentially in time for all three test problems. The errors either reach steady values or grow with much smaller rates with increasing time.

3.3. *Effect of material properties*

The effect of material properties in static tests was studied in Section 3.1. To study the effect of material properties more thoroughly in dynamic tests, we consider the impact problem introduced in Section 3.2. Norms of errors at the final time, $t = 0.15$, are compiled for several values of density and shear modulus ratios in Figures 6. In general, errors are larger for materials with larger property ratios. For fixed $R_\mu = 1$, the errors seem to saturate at $R_\rho \approx 10$ to values around 0.001-0.006 depending on the physical quantity considered and do not increase much as R_ρ is increased further. Over the range of shear modulus ratios investigated, the errors do not saturate, but continue to increase,

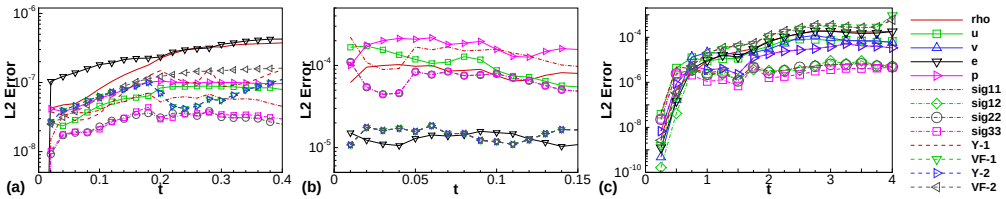

FIGURE 5. Temporal evolution of relative errors in different quantities in dynamic tests. Results from (a) relaxation test, (b) impact problem, and (c) two-dimensional copper-aluminum Richtmyer-Meshkov problem.

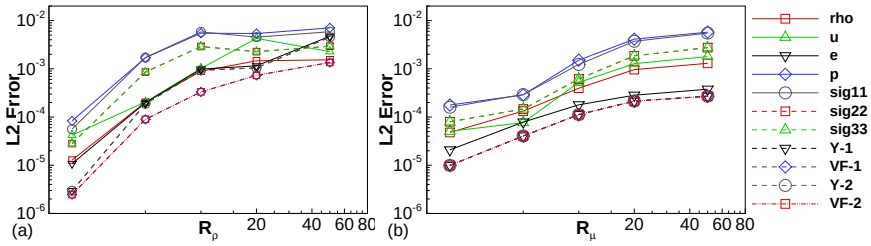

FIGURE 6. Effect of material equation of state parameters on the errors in the impact problem. (a) Varying R_ρ with $R_\mu = 1$. (b) Varying R_μ with $R_\rho = 1$. Numerical parameters are $\alpha_{min} = 10^{-6}$ and $\delta_t = 3.0$ with $NX = 101$.

as R_μ is increased, with $R_\rho = 1$ kept fixed. These trends are consistent with the static test results shown in Figure 1(c).

3.4. *Effect of numerical parameters*

The trends in the static tests suggest that, in addition to the material EOS parameters, the errors in the mixture formulation are dependent on the volume fractions encountered. The volume fractions encountered in a numerical simulation are dependent on two numerical parameters, namely, the minimum volume fraction, α_{min}, used to denote absence of a material, and the thickness of the interface, δ_t. Sensitivity to these numerical parameters is evaluated here with the elastic-plastic impact problem. The precise definitions of α_{min} and δ_t are given in Section 3.2.

Two material combinations of practical interest, Cu-Al and Cu-water, are considered. The properties of Al are the same as those used in Section 3.2, while slightly different values are used for Cu. The EOS parameter values used for Cu are $\gamma = 4.22$, $p_\infty = 30.8$ GPa, $\mu = 43.3$ GPa, $\sigma_Y = 0.45$ GPa and $\rho_0 = 8930$ kg/m^3. The corresponding values for water are $\gamma = 4.4$, $p_\infty = 0.6$ GPa, $\mu = 0$ GPa, $\sigma_Y = 0$ GPa, $\rho_0 = 1000$ kg/m^3. It may be noted that the property ratios are significantly larger for Cu-water than for Cu-Al.

Figure 7 shows that varying α_{min} over six orders of magnitudes has practically no influence on the errors in different quantities, for both material combinations. The number of points used is $NX = 101$, which implies five grid points in the interface for $\delta_t = 1$ and eleven grid points for $\delta_t = 3.5$. Similar to the effect of α_{min}, the material interface thickness parameter has a weak effect on the errors.

To summarize the results of this section, the errors introduced by the mixture formulation, with the multiple-g formulation results considered as benchmarks, are dependent primarily on the material properties involved. The evolution of errors in time as well as dependence on numerical parameters is small.

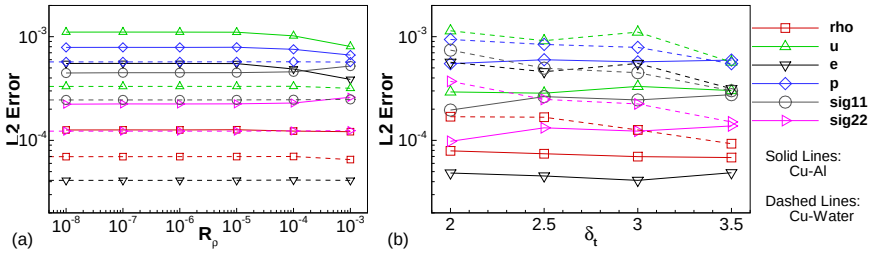

FIGURE 7. Effect of numerical parameters on the errors in copper-aluminum and copper-water impact problems. Relative error norms with varying (a) α_{min} and (b) δ_t at the final non-dimensional time, $t = 0.15$.

4. Application of the mixture formulation

The performance of the mixture formulation was compared to that of the multiple-g formulation in the previous section. Numerical regularization of shocks and material interfaces leads to weak spurious waves that are present in the multiple-g formulation as well as in the mixture formulation. Errors computed with the multiple-g formulation result as a benchmark are thus contaminated to some extent by these spurious numerical artifacts. Hence, it is important that the mixture formulation be evaluated against other benchmark solutions as well. In this section, we consider a linear longitudinal wave interacting with an interface between two elastic solids, and a Taylor rod-on-rod impact problem. The results of the mixture formulation are compared to an exact analytical solution and a very finely resolved numerical solution for the first problem, and to an experiment for the second problem.

4.1. *Convergence*

We consider two materials with properties $\gamma_1 = \gamma_2 = 1.4$, $p_{\infty,1} = p_{\infty,2} = 1$, $\mu_1 = \mu_2 = 1$, $\rho_{0,1} = 1$ and $\rho_{0,2} = 0.5$. These parameters have been non-dimensionalized with $p_{\infty,1}$ and $\rho_{0,1}$ as pressure and density scales. The domain is periodic on $x \in [0, 1)$, with a slab of material 2 initialized in $x \in [0.5, 0.9]$. The initial volume fraction profiles are as described in the first test problem in Section 3.2, with interface thickness parameter δ_t and physical thickness $\delta_t \Delta x$. A compression plane-strain wave moving to the right is initialized at $x = 0.35$. The normal stress profile for such a wave is $\sigma_{11} = -\sigma_0 \exp\left[-\left(\left(x - c_{L,1}t - 0.35\right)/0.035\right)^2\right]$, where $c_{L,1} = \sqrt{\left(\gamma_1 p_{\infty,1} + 4\mu_1/3\right)/\rho_{0,1}}$ is the linear longitudinal wave speed in material 1, and $\sigma_0 = 10^{-4}$. The strength of the wave, controlled by σ_0, is small enough that the linear solution is a good approximation to the non-linear problem.

The stress profiles of the initial condition, and the reflected and transmitted waves at $t = 0.2$ are shown in Figure 8(a). It is clear that with an increasing number of grid points, the numerical solution approaches the exact solution denoted by the symbols. Norms of errors computed over the subdomain $x \in [0.05, 0.3]$, to isolate the reflected wave, are plotted in Figure 8(b). Keeping the interface thickness parameter, δ_t, fixed at 1, the interface thickness, $\delta_t \Delta x$, reduces proportional to $1/NX$. In other words, the numerically diffuse interface approaches a sharp interface at first order. An exact solution to the sharp-interface problem may be found in classical textbooks of elasticity (e.g., Achenbach (1975)). The diffuse-interface numerical solution approaches this analytical solution that is strictly applicable only in the sharp-interface limit at second order. Contrastingly, keeping the physical thickness of the interface, $\delta_t \Delta x$, fixed at 0.01 and considering a very

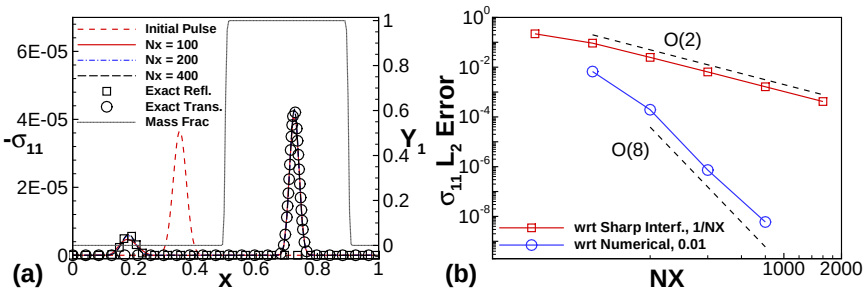

FIGURE 8. Convergence of the mixture formulation demonstrated for a Gaussian pulse-interface interaction problem. (a) Profiles of non-dimensional axial stress, $-\sigma_{11}$, and mass fraction, Y_1. Numerical solution using different grid sizes denoted by lines. Exact solution denoted using symbols, with reflected and transmitted waves denoted distinctly. (b) Error analysis with respect to the exact analytical solution for the sharp-interface problem with interface thickness $1/NX$ and with respect to the numerical solution using $NX = 12800$ with interface thickness 0.01.

finely resolved numerical solution as the benchmark, the errors are seen to reduce at eighth order. This is consistent with the underlying numerical scheme.

The mixture formulation is seen to converge to the appropriate reference solutions with a high order of accuracy. The orders of accuracy shown by the mixture formulation are identical to those obtained for a similar problem using the multiple-g formulation, as was reported by Subramaniam *et al.* (2017).

4.2. *Taylor rod-on-rod impact*

The final demonstration problem is a classical Taylor rod-on-rod impact. A cylindrical Cu rod of radius 5 mm and height 100 mm impacts another identical rod with a velocity of ± 197.5 m/s. The material properties for Cu used here follow from Hank *et al.* (2017), and are $\gamma_1 = 4.54$, $p_\infty = 29.9$ GPa, $\mu = 48.5$ GPa, $\sigma_Y = 0.45$ GPa and $\rho_0 = 8924$ kg/m^3. The Cu rod is assumed to be surrounded by water, with properties as given in Section 3.4. This cylindrically symmetric problem is simulated in cylindrical coordinates with $z \in [0, 120]$ mm $\times$ $r \in [0, 20]$ mm. The impact occurs at $z = 0$. Symmetric boundary conditions are applied at the $z = 0$ and $r = 0$ boundaries, while non-reflecting sponge layers are maintained at $z = 120$ mm and $r = 20$ mm.

The impact at $z = 0$ and $t = 0$ leads to elastic-plastic shocks that propagate from the point of impact, and undergo a series of reflections and transmissions from the Cu-water interface. The net effect of these interactions is the formation of a bulge at the base of the rod, and the eventual attainment of a stationary state. Profiles of the rod radius as a function of the distance from the point of impact are shown in Figure 9 for different time points, along with experimental results reported by Forde *et al.* (2009). While the experiments employed air as the medium surrounding the Cu rod, water is used in our simulations. Additional simulations exploring the effect of surrounding medium were carried out, and the rod deformations were not found to be very sensitive to the surrounding medium.

Figure 9 shows that the results agree reasonably well with experiments. The agreement improves with increasing grid resolution. The discrepancies between the simulations and experiments can be attributed to the fact that the perfectly-plastic model with instantaneous relaxation is used here. As a result, strain-hardening effects are absent from the current formulation. Nevertheless, the level of agreement obtained with the experimen-

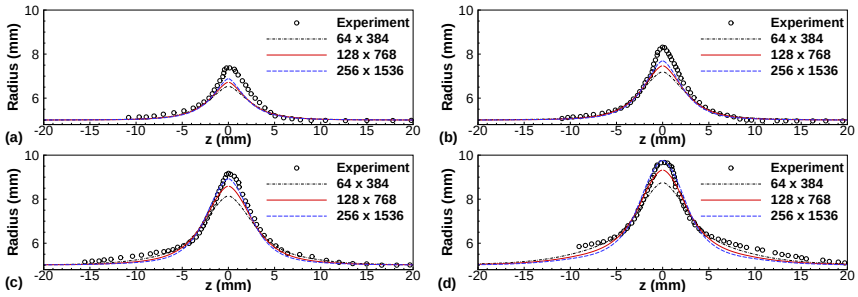

FIGURE 9. Taylor rod-on-rod impact problem results using the mixture formulation and a comparison to experiments by Forde *et al.* (2009). Profiles of rod radius as a function of distance from point of impact for times (a) 12, (b) 20, (c) 36 and (d) 52 μs. Legend denotes the grid resolution in r and z directions. Numerical results are reflected assuming symmetry about $z = 0$.

tal results indicates that the mixture formulation can be used for problems of practical interest.

5. Conclusions

We have developed a reduced form of a multi-material formulation capable of handling non-linear elastic-plastic deformations of solids and fluids. In contrast to the full (multiple-g) formulation involving multiple fields of inverse deformation gradient tensors, the reduced formulation relies on only one inverse deformation gradient tensor field. This formulation is termed the 'mixture' multi-material formulation, and results in a system of only $M + 13$ governing equations for a problem involving M materials, in contrast to a system of $10M + 4$ equations for the full multi-material formulation.

The differences between the mixture formulation and the multiple-g formulation can be attributed to different $\underline{\boldsymbol{g}}^e$ fields caused by material properties as well as to mass-consistency errors introduced by the numerical solution methodology. Assessment on one-dimensional and two-dimensional problems shows that the errors do not grow rapidly in time, and that they are primarily confined to regions of sharp gradients, such as close to shocks or material interfaces. The material EOS parameter values primarily control the errors in the mixture formulation with respect to the multiple-g formulation. Numerical parameters such as the minimum volume fraction and the thickness of the material interfaces have limited influence on the errors. Finally, the mixture formulation behaves similarly to the multiple-g formulation with respect to convergence on grid refinement. The mixture formulation also yields reasonable agreement with experimental results on a classical Taylor rod-on-rod impact test.

The Eulerian multi-material mixture formulation developed and analyzed here enables accurate simulations at a much-reduced cost for certain material combinations. Future work will focus on incorporation of advanced plasticity effects such as strain hardening and thermal softening, and more complex problems involving more than two materials.

Acknowledgments

This work was performed under the auspices of the U.S. Department of Energy by Lawrence Livermore National Laboratory under Contract DE-AC52-07NA27344.

REFERENCES

Achenbach, J. D. 1975 *Wave Propagation in Elastic Solids*. Elsevier.

Benson, D. J. 1992 Copmutational methods in Lagrangian and Eulerian hydrocodes. *Comput. Methods Appl. Mech. Eng.* **99**, 235–394.

Brouillette, M. 2002 The Richtmyer-Meshkov instability. *Annu. Rev. Fluid Mech.* **34**, 445–468.

Cook, A. W. 2009 Enthalpy diffusion in multicomponent flows. *Phys. Fluids* **21**, 055109.

Cook, A. W. & Cabot, W. H. 2005 Hyperviscosity for shock-turbulence interactions. *J. Comput. Phys.* **203**, 379–385.

Donea, J., Huerta, A., Ponthot, J.-P. & Rodrguez-Ferran, A. 2004 *Arbitrary Lagrangian-Eulerian Methods*. John Wiley & Sons, Ltd.

Favrie, N. & Gavrilyuk, S. L. 2010 Dynamics of shock waves in elastic-plastic solids. *Proc. ESAIM* pp. 1–18.

Favrie, N. & Gavrilyuk, S. L. 2012 Diffuse interface model for compressible fluid - compressible elastic-plastic solid interaction. *J. Comput. Phys.* **231**, 2695–2723.

Forde, L. C., Proud, W. G. & Walley, S. M. 2009 Symmetrical Taylor impact studies of copper. *Proc. R. Soc. A* **465**, 769–790.

Ghaisas, N. S., Subramaniam, A. & Lele, S. K. 2016 High-order Eulerian methods for elastic-plastic flow in solids and coupling with fluid flows. *AIAA Paper* #2016-3350.

Godunov, S. K. & Romenskii, E. I. 2003 *Elements of Continuum Mechanics and Conservation Laws*. Springer.

Hank, S., Gavrilyuk, S. L., Favrie, N. & Massoni, J. 2017 Impact simulation by an Eulerian model for interaction of multiple elastic-plastic solids and fluids. *Int. J. Impact Eng.* **100**, 104–111.

Kennedy, C. A., Carpenter, M. H. & Lewis, R. M. 2000 Low-storage, explicit Runge–Kutta schemes for the compressible Navier–Stokes equations. *App. Numer. Math.* **35**, 177–219.

Lele, S. K. 1992 Compact finite difference schemes with spectral-like resolution. *J. Comput. Phys.* **103**, 16–42.

López Ortega, A., Lombardini, M., Pullin, D. I. & Meiron, D. I. 2014 Numerical simulation of elastic-plastic solid mechanics using an Eulerian stretch tensor approach and HLLD Riemann solver. *J. Comput. Phys.* **257**, 414–441.

Miller, G. H. & Colella, P. 2001 A high-order Eulerian Godunov method for elastic-plastic flow in solids. *J. Comput. Phys.* **167**, 131–176.

Ndanou, S., Favrie, N. & Gavrilyuk, S. L. 2015 Multi-solid multi-fluid diffuse interface model: Applications to dynamic fracture and fragmentation. *J. Comput. Phys.* **295**, 523–555.

Plohr, B. & Sharp, D. 1989 A conservative Eulerian formulation of the equations for elastic flow. *Adv. Appl. Math.* **9**, 481–499.

Subramaniam, A., Ghaisas, N. S. & Lele, S. K. 2017 High-order Eulerian simulations of multi-material elastic-plastic flow. *J. Fluid. Eng.* (In Press), doi: 10.1115/1.4038399.

Trangenstein, J. A. & Colella, P. 1991 A higher-order Godunov method for modelling finite deformation in elastic-plastic solids. *Commun. Pur. Appl. Math.* **44**, 41–100.